

# Simultaneous inversion for microseismic event location and velocity model in Vaca Muerta Formation

Zhishuai Zhang<sup>1</sup>, Jing Du<sup>2</sup>, and Fuchun Gao<sup>2</sup>

## ABSTRACT

Velocity models play a key role in locating microseismic events; however, it is usually challenging to construct them reliably. Traditional model-building strategies depend on the availability of well logs or perforation shots. We simultaneously invert for microseismic event locations and a velocity model under the Bayesian inference framework, and we apply it in a field data set acquired in the Vaca Muerta Formation at Neuquén, Argentina. This methodology enables uncertainty and posterior covariance analysis. By matching the moveouts of the P- and S-wave arrival times, we were able to estimate a 1D velocity model to achieve improved event locations. Various analyses indicate the superiority of this model over a model built with the traditional strategy. With this algorithm, we can perform microseismic monitoring to fracturing treatments in which no perforation data are available. In addition, we can also apply it for long-term passive seismicity reservoir monitoring in which changes of reservoir properties are expected.

## INTRODUCTION

Multistage fracturing techniques, together with horizontal drilling, make economic production from organic-rich shale possible. Microseismic monitoring of hydraulic fractures has been an important technology for far-field fracture diagnostics (Eisner and Le Calvez, 2007; Maxwell, 2014). It can provide hydraulic-fracture geometry and its growth over time. Getting accurate event locations is important to microseismic interpretation. Various methods originally developed for earthquake location have been used in microseismic processing, such as traveltimes inversion (Aki and Richards,

1980; Rutledge and Phillips, 2003), the double-difference method (Waldhauser and Ellsworth, 2000), coherence scanning (Drew et al., 2005; Duncan and Eisner, 2010), time-reverse imaging (Artman et al., 2010; Artman and Witten, 2011), and waveform inversion (Song and Toksöz, 2011). In all of these methods, the velocity model plays a key role (Eisner et al., 2009; Maxwell, 2009; Warpinski, 2009; Li et al., 2012; Gesret et al., 2015). However, due to the limited number of perforation shots, limited ray coverage, and difficulty in picking S-wave arrivals reliably in the perforation data, building a reasonable velocity model is usually challenging (Maxwell, 2014).

Simultaneous inversion of earth model and earthquake locations has been successfully used in earthquake seismology (Douglas, 1967). The limitation of acquisition geometry and low signal-to-noise ratio (S/N) make it challenging to apply it to microseismic data. There are a few studies about it for microseismic event locations (Grechka and Heigl, 2017). Jansky et al. (2010) use the neighborhood algorithm to invert for event locations and a velocity model in a downhole survey. Zhang et al. (2009) have used the double-difference tomography method to study the induced seismicity monitored with geophones deployed in five monitoring wells. Li et al. (2013, 2014) simultaneously invert for Thomsen parameters and event locations using P- and S-wave arrival time information. Grechka et al. (2011) estimate key stiffness coefficients that can be well-constrained by assuming a homogeneous earth model. Grechka and Yaskevich (2014) demonstrate the feasibility of simultaneous inversion for event locations and azimuthal anisotropic layered model with a Bakken case study. However, the study of simultaneous inversion in the microseismic industry is still very limited, especially for the cases in which acquisition geophones are confined within one single well.

Bayesian inference is a powerful statistical tool to integrate the observations into a prior probability of model parameters to obtain the posterior probability (Tarantola, 2005; Box and Tiao, 2011). Even though usually suffering from difficulties in choosing prior

Manuscript received by the Editor 5 January 2017; revised manuscript received 10 October 2017; published ahead of production 24 January 2018; published online 13 April 2018.

<sup>1</sup>Formerly University of California, Department of Civil and Environmental Engineering, Berkeley, California, USA; presently Stanford University, Department of Geophysics, Stanford, California, USA. E-mail: zhishuaizhang@gmail.com.

<sup>2</sup>Total E&P Research and Technology, LLC, Houston, Texas, USA. E-mail: jing.du@total.com; fuchun.gao@total.com.

© 2018 Society of Exploration Geophysicists. All rights reserved.

probability and intensive computational effort, it has been widely used in subsurface inverse problems (Tarantola and Valette, 1982; Tarantola, 2005; Myers et al., 2007, 2009; Poliannikov et al., 2013, 2014; Zhang et al., 2014). We have developed a Bayesian inference framework for simultaneous inversion and successfully applied it to a data set acquired from shallow borehole stations in the Newberry enhanced geothermal system (EGS) (Zhang et al., 2017). Studies show that a velocity model can be constructed with relatively high confidence using microseismic data only. The Bayesian inference provides an efficient way to quantify the uncertainty of the inversion. It is also able to capture the correlation between various model parameters, such as velocity and event location.

In this paper, we applied the simultaneous inversion algorithm to a data set acquired in a single observation well within the Vaca Muerta Formation at Neuquén, Argentina. Bayesian inference is successful in integrating various information in the inversion for this data set. The uncertainty is obtained and compared with an arrival time misfit map. Correlation matrix among various parameters has been calculated and discussed. A comparison with a traditional location result is presented. Analyses with angle of incidence, arrival time match, and perforation shots show the advantages of this method. The simultaneous inversion minimizes the requirement of a predetermined velocity model and provides the possibility to study the time lapse change of the earth due to hydraulic fracturing.

The structure of the remainder of this paper is as follows: We first give an overview of the simultaneous inversion algorithm, followed by the introduction of the microseismic survey and the initial model used for inversion. The developed algorithm is then applied to a data set from the Vaca Muerta formation, and the results are verified with various analyses. We also study the potential of capturing

time-lapse changes or lateral variation of the earth. Finally, we conclude with a discussion of the limitations and next steps of this work.

### METHODS

The Bayesian inference framework for simultaneous inversion has been successfully applied to a shallow borehole microseismic survey in Newberry EGS (Zhang et al., 2017). In this section, we apply this method to a survey acquired in a vertical observation well, which is a typical microseismic acquisition geometry.

As a common practice in the microseismic industry (Grechka and Yaskevich, 2013; Li et al., 2014; Maxwell, 2014), we assume a 1D layered isotropic velocity model. Given the relatively small scale that a microseismic survey usually involves and the small lateral heterogeneity for a typical unconventional reservoir, this is usually a valid assumption. In cases in which lateral heterogeneity needs to be considered, stage-dependent velocity models can be built. Under this assumption, along with the fact that the geophones are in a vertical monitoring well, 3D microseismic location using arrival times can be transformed into a 2D problem plus an azimuth estimation problem. In the 2D problem, an event is characterized by the horizontal source-receiver distance and its elevation. The parameterization of the earth model can be challenging. More parameters will decrease the parameterization error; however, this may make the inverse problem underdetermined. The velocity parameter set we choose in this study is comprised of P- and S-wave velocities. However, depending on the data quality, raypath coverage, and availability of the prior information, parameters with various levels of

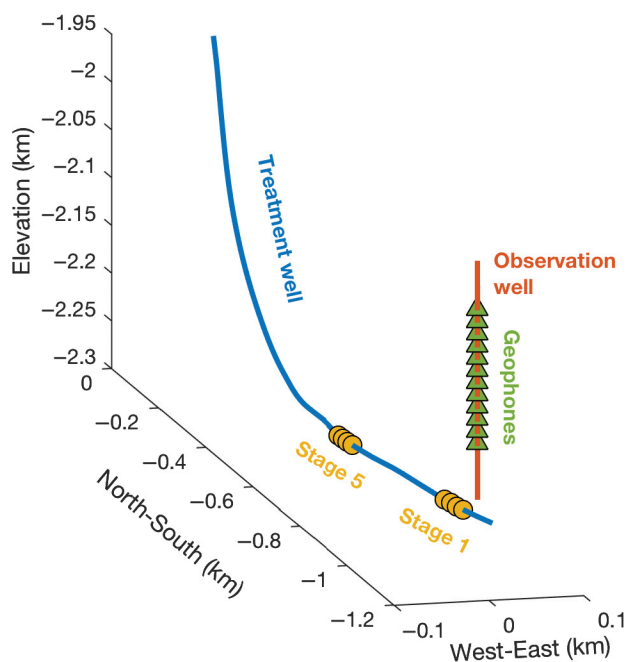


Figure 1. Stimulation project and microseismic survey setup. In total, five treatment stages were performed in the horizontal stimulation well. Microseismic data from stage 1 and stage 5 were acquired and studied. The microseismic monitoring was carried out by a 24-tool, 12-level double-stacked receiver array positioned in the adjacent vertical observation well.

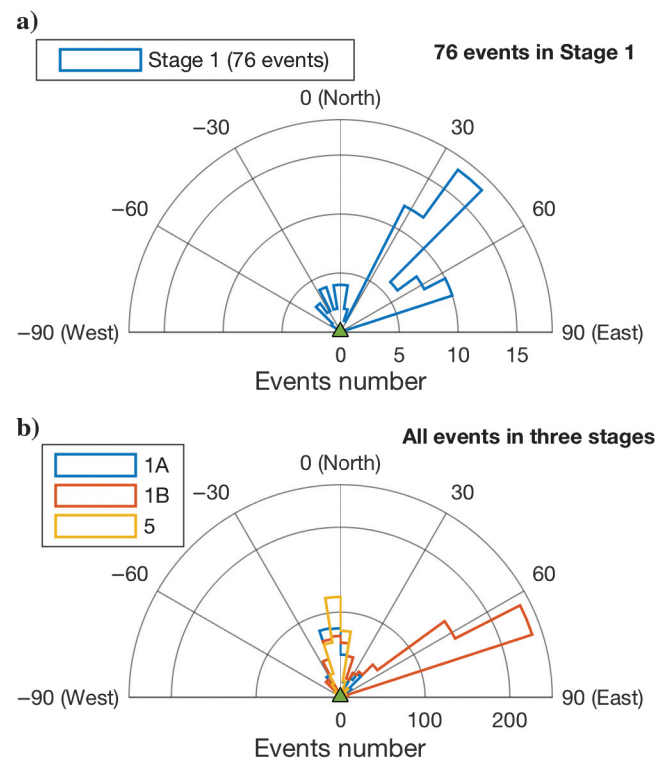


Figure 2. Azimuthal coverage of the analyzed events. (a) Azimuthal coverage of the 76 events used in the 2D study and (b) azimuthal coverage of the entire data set in each stage.

complexity, including layer boundary elevations and anisotropic parameters, may be used. In this study, for a system with  $N$  microseismic events and  $M$  layers, the model parameter set  $\mathbf{m}$  consists of  $3N + 2M$  elements:

$$\mathbf{m} = [\mathbf{x}_1, \mathbf{x}_2, \dots, \mathbf{x}_i, \dots, \mathbf{x}_N; V_{P1}, V_{S1}, V_{P2}, V_{S2}, \dots, V_{Pj}, V_{Sj}, \dots, V_{PM}, V_{SM}]^T, \quad (1)$$

where  $\mathbf{x}_i = [H_i, E_i, t_i]$  are the horizontal source-receiver distance  $H_i$ , event elevation  $E_i$ , and origin time  $t_i$  of the  $i$ th event. The terms  $V_{Pj}$  and  $V_{Sj}$  are the P- and S-wave velocities of the  $j$ th layer of the earth model. Including layer boundary elevations in the model parameters may cause the inversion to be ill-posed given the possible trade-offs between nearby layers. Thus, we fixed the boundary elevations during the inversion, which is the same practice in most other related studies (Grechka et al., 2011; Grechka and Yaskevich, 2013; Li et al., 2014).

The observation vector  $\mathbf{d}_{\text{obs}}$  includes any available P- and S-wave arrival times. The forward operator  $\mathbf{g}(\cdot)$  is to predict the observable parameters using a given set of model parameters  $\mathbf{m}$ . Specifically, it calculates the phase arrival times at all geophone locations using a ray-tracing method.

According to inverse theory (Tarantola, 2005; Zhang et al., 2017), under a Gaussian assumption the posterior probability density of model parameters is given by

$$\sigma_M(\mathbf{m}) = c \exp \left\{ -\frac{1}{2} [\mathbf{g}(\mathbf{m}) - \mathbf{d}_{\text{obs}}]^T \mathbf{C}_D^{-1} [\mathbf{g}(\mathbf{m}) - \mathbf{d}_{\text{obs}}] - \frac{1}{2} (\mathbf{m} - \mathbf{m}_{\text{prior}})^T \mathbf{C}_M^{-1} (\mathbf{m} - \mathbf{m}_{\text{prior}}) \right\}, \quad (2)$$

where  $\mathbf{m}_{\text{prior}}$  is the prior mean values of the model parameters. The covariance matrix  $\mathbf{C}_D$  is the summation of the measurement uncertainty  $\mathbf{C}_d$  and the parameterization uncertainty  $\mathbf{C}_T$ . The function  $\mathbf{C}_M$

is the covariance matrix of the prior information and  $c$  is a normalization constant. A detailed discussion of equation 2 is presented by Tarantola (2005) and Zhang et al. (2017).

Following the strategy of Zhang et al. (2017), we use the maximum a posterior (MAP) estimation  $\mathbf{m}_{\text{MAP}}$ , along with its covariance matrix  $\mathbf{C}_{\mathbf{m},\text{MAP}}$  to characterize the posterior probability density of model parameters:

$$\mathbf{m}_{\text{MAP}} = \arg \max_{\mathbf{m}} \sigma_M(\mathbf{m}) \quad (3)$$

and

$$\mathbf{C}_{\mathbf{m},\text{MAP}} = \mathbf{C}_M - \mathbf{C}_M \mathbf{G}_{\text{MAP}}^T (\mathbf{G}_{\text{MAP}} \mathbf{C}_M \mathbf{G}_{\text{MAP}}^T + \mathbf{C}_D)^{-1} \mathbf{G}_{\text{MAP}} \mathbf{C}_M, \quad (4)$$

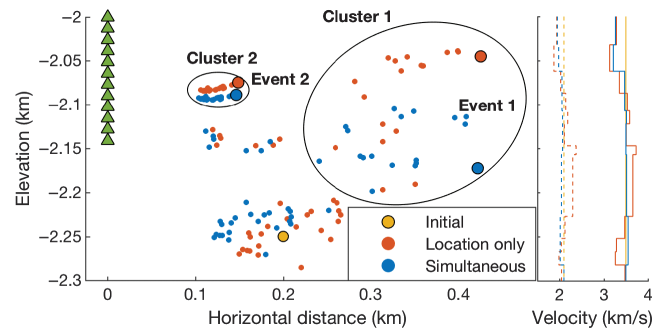


Figure 4. The prior/initial event location (yellow dot), locations estimated by simultaneous inversion (blue dots) and the traditional method (orange dots). The right panel shows the prior/initial velocity model (yellow lines), the model simultaneously estimated (blue lines) and the one provided by the contractor (orange lines). The solid lines are for  $V_P$  and the dashed lines are for  $V_S$ . The SD of the prior event location is 1.0 km in the horizontal and vertical directions. The SD of the prior velocity model is 2.0 km/s for P- and S-waves.

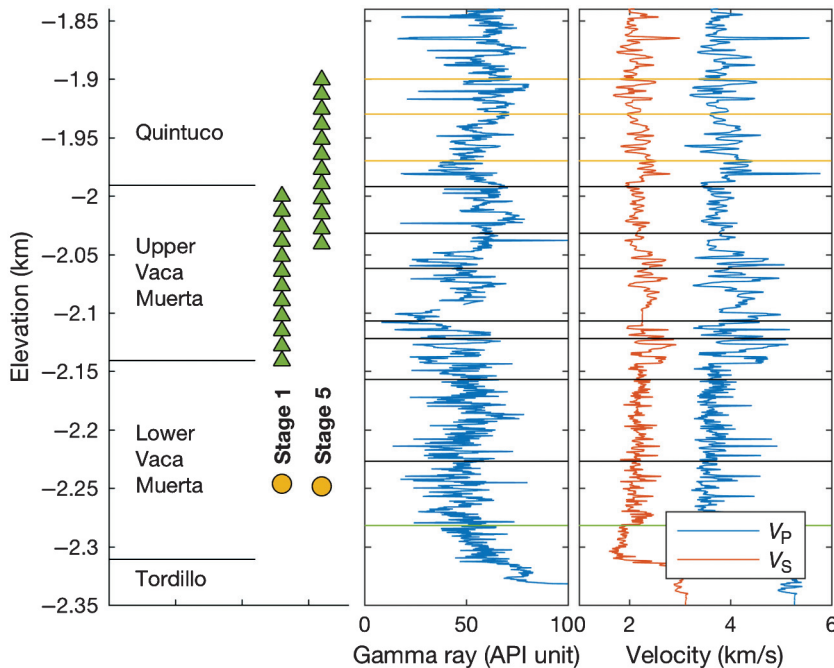


Figure 3. The prior/initial velocity models we used for simultaneous inversion are 1D multilayer models. The layer interfaces are positioned based on the sonic logs, geologic information, and the contractor's model. The green triangles and yellow circle on the left panel indicate the elevations of geophones and perforation shots, respectively. The black and green lines on the logs indicate the layer interfaces for the stage 1 velocity model. The black and yellow lines are for the stage 5 model.

where  $\mathbf{G}_{MAP}$  is the sensitivity matrix with elements  $G_{ij} = \partial g_i / \partial m_j$  at the MAP point.

Even though the MAP estimation is exact only when all the information is of the Gaussian type and the operator  $\mathbf{g}(\cdot)$  is linear, which is usually not the case, it is efficient in terms of computation and is normally a reasonable representation of the posterior probability density. In this study, the  $\mathbf{m}_{MAP}$  is achieved with a Gauss-Newton method (Zhang et al., 2017).

### MICROSEISMIC SURVEY OVERVIEW

The hydraulic fracturing was performed in the Vaca Muerta Formation at Neuquén, Argentina. Its acquisition geometry is shown in Figure 1. The Vaca Muerta is of Jurassic and Cretaceous age. It is located at the eastern foothills of the Andean range and the western side of the Colorado Basin. It covers a total area of 160,000 km<sup>2</sup> (Garcia et al., 2013). Its thickness ranges from 60 to more than 800 m, with average values of 200–300 m (Rohmer et al., 2015). The Vaca Muerta Formation consists of an upper (elevation of -1.985 to -2.135 km in the studied area) and a lower (elevation of -2.135 to -2.305 km in the studied area) member. It is overlain by the Quintuco Formation (elevation of -1.221 to -1.985 km) and

above the Tordillo Formation (below the elevation of -2.305 km). The upper Vaca Muerta is composed of calcareous shales, marls, and micritic limestones with variable total organic carbon content. The lower member is mainly organic-rich shales. Thin layers of siltstone, very fine-grained sandstone, and fine-grained volcanoclastic deposits are occasionally found (Sagasti et al., 2014). The Quintuco Formation is mainly composed of carbonate, and the Tordillo Formation is mainly composed of sandstone.

The horizontal stimulation well is perpendicular to the expected fracture azimuth in the lower Vaca Muerta. It is completed as a cemented lateral using a plug-and-perf. In total, five hydraulic fracturing treatment stages were performed. Due to an operational issue, stage 1 was pumped twice, which are referred to as stage 1A and stage 1B. The microseismic data were acquired by a 24-tool, 12-level double-stacked geophone array positioned in a vertical well. The sampling rate of the recording is 0.25 ms. Among the five stimulation stages, microseismic data from only stage 1 and stage 5 were acquired. The geophone array was moved approximately 100 m shallower from stage 1 to stage 5. The numbers of triggered events in stages 1A, 1B, and 5 are 404, 884, and 377, respectively. Among all the perforation shots for the five stages, only the last three shots for stage 1 were recorded.

The data have been processed by a contractor using standard industrial practice. In the contractor’s processing, an initial 1D layered isotropic velocity model was built based on a sonic log. Then, it was calibrated with perforation shots and early microseismic events. The event locations were estimated by minimizing the misfit between the picked and predicted arrival times. The forward modeling was conducted by solving eikonal equation for the first arrivals, which might be direct or refracted (head) waves.

### PREPROCESSING AND INITIAL MODEL

To prepare for inversion, we selected 76 events from stage 1 to repick the arrival times. The selection criteria mainly depend on S/N and raypath coverage. Figure 2a shows the azimuthal coverage of these 76 events. To ensure the quality of the picking, we rotated the waveforms to separate P-, SH-, and SV-wave components. The

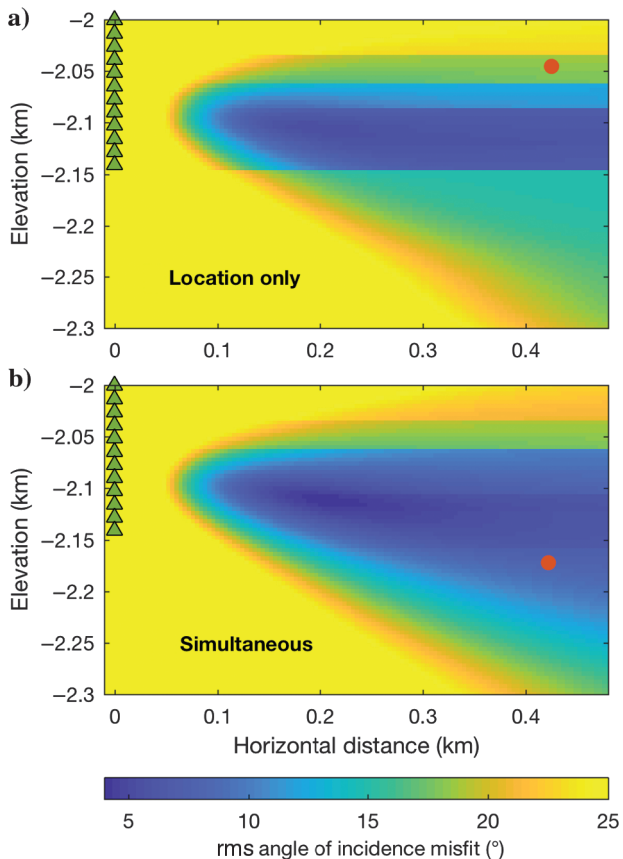


Figure 5. An rms angle of incidence misfit map for event 1 in Figure 4. (a) The velocity model used is provided by the contractor. The orange dot denotes the location estimated by the traditional method. It gives a relatively large angle of incidence misfit of 18°. (b) The velocity model used is estimated with simultaneous inversion. The orange dot denotes the location estimated simultaneously. It lies within an area of a small angle of incidence misfit of 8°.

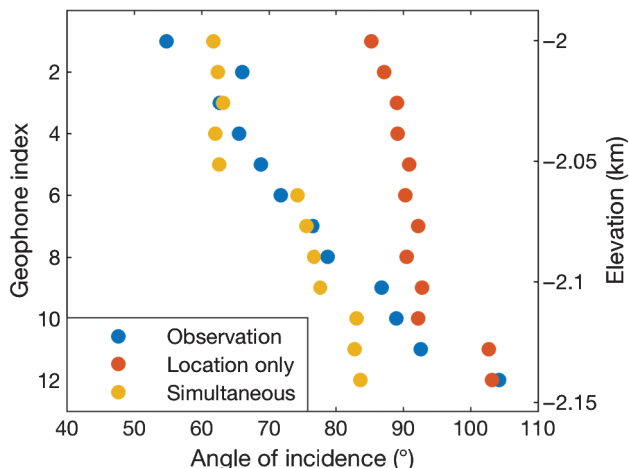


Figure 6. The observed and predicted angle of incidence at each geophone location. The traditional location method results in a relatively large difference from the observed angles. The simultaneous inversion provides an improved match with the observation.

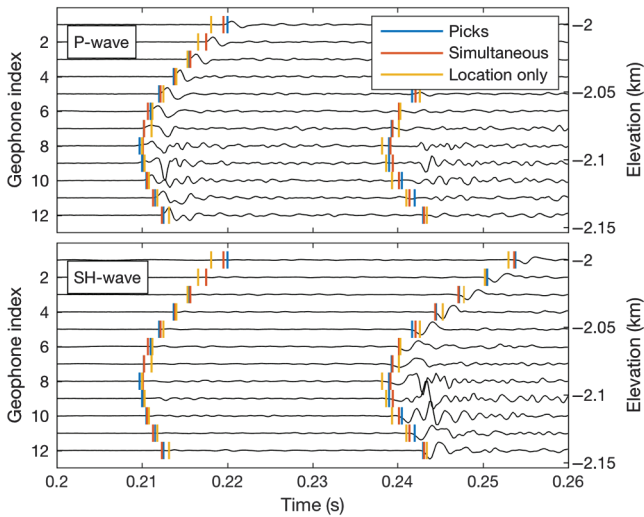


Figure 7. The P- and SH-component waveform of event 2 in Figure 4. The blue lines stand for manually picked arrival times. The orange lines are predictions of simultaneous inversion. The yellow lines are predictions of the traditional method. The P- and S-wave arrival times predicted by the traditional method are unable to match the arrival time picks. The simultaneous inversion was able to improve this match.

orientations of geophones have been calibrated by the contractor using perforation and check shots. We picked P-wave arrival times from the P-wave component and S-wave arrival times from the SH-wave component whenever we were able to do so. We used our own pickings for the following processing unless stated otherwise.

We built a 9-layer homogeneous prior model for stage 1 and an 11-layer model for stage 5. The layer interfaces are positioned based on the sonic logs, gamma ray logs, geologic information, and the contractor’s velocity model (Figure 3). The prior mean values of  $V_P$  and  $V_S$  are 3.5 and 2.1 km/s, respectively. Their standard deviations (SDs) are both 2.0 km/s. This relatively large value ensures that the inversion is insensitive to the prior mean  $V_P$  and  $V_S$  value. The same philosophy applies for other prior information such as event locations and origin times. The prior mean horizontal source-receiver distances are 0.2 km for all stage 1 events and 0.4 km for all stage 5 events. The prior mean elevations of all events are  $-2.25$  km. The location SDs in both directions are 1.0 km. The yellow dot and lines in Figure 4 show the prior mean event location and velocity model for stage 1, respectively. The plot of prior information for stage 5 is not shown here for simplicity. The prior mean origin times are 0.2 s before the first P-wave arrival time with a SD of 8.0 s. The minimization of the objective function starts with the prior mean values as the initial model in all of the experiments.

Table 1. Mean, SD, and rms of misfits in various experiments.

| Events           | Velocity model type        | Mean misfit (ms) |       |         | SD of misfits (ms) |      |         | Rms misfit (ms) |      |         |
|------------------|----------------------------|------------------|-------|---------|--------------------|------|---------|-----------------|------|---------|
|                  |                            | P                | S     | P and S | P                  | S    | P and S | P               | S    | P and S |
| 76 events        | Contractor                 | 0.06             | -0.14 | -0.04   | 1.31               | 1.98 | 1.68    | 1.31            | 1.98 | 1.68    |
|                  | 76 events estimated        | -0.02            | -0.02 | -0.02   | 0.42               | 0.51 | 0.46    | 0.42            | 0.51 | 0.47    |
| First 38 events  | First 38 events estimated  | -0.02            | -0.02 | -0.02   | 0.38               | 0.48 | 0.44    | 0.38            | 0.48 | 0.44    |
|                  | Second 38 events estimated | -0.02            | -0.02 | -0.02   | 0.41               | 0.50 | 0.46    | 0.41            | 0.50 | 0.46    |
| Second 38 events | Second 38 events estimated | -0.02            | -0.02 | -0.02   | 0.44               | 0.52 | 0.48    | 0.44            | 0.52 | 0.48    |
| Three perfs      | 76 events estimated        | -0.03            | -0.02 | -0.03   | 1.00               | 0.77 | 0.89    | 0.99            | 0.76 | 0.88    |

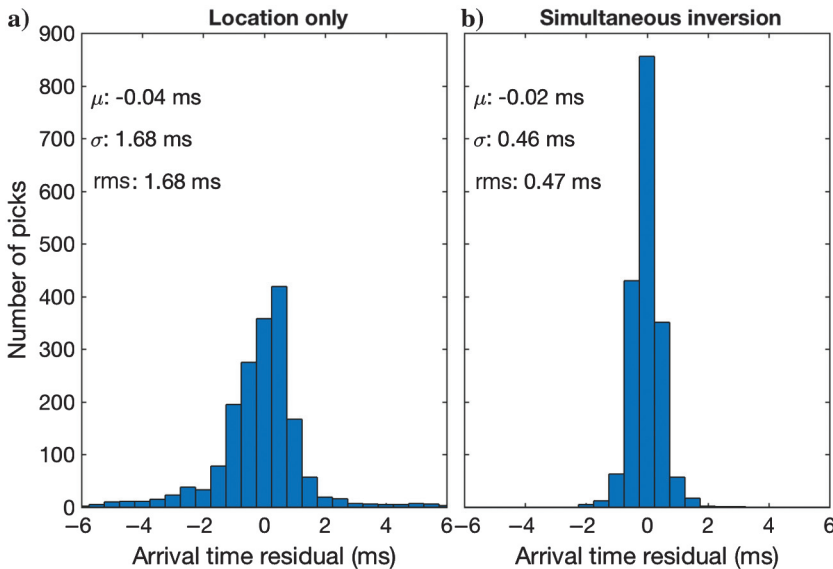


Figure 8. The histogram of misfits between the observed and predicted arrival times. The misfits of the simultaneous inversion (b) are more concentrated around zero than those of the traditional method (a).

We use a SD of 1.5 ms to represent the measurement and parameterization uncertainties to calculate  $C_D$  in equation 2.

### INVERSION RESULT

#### Traditional location with the contractor-provided velocity model

For the purpose of comparison, we first locate the 76 events with the velocity model provided by the contractor using a traditional location method. Specifically, we used the same program as the simultaneous inversion, but the velocity model is not updated. The location result is similar to that provided by the contractor, which is not shown here for simplicity. We use this location result with the provided velocity model as a typical result by a traditional location method for comparison purposes.

#### Simultaneous inversion

We located these 76 event locations with the simultaneous inversion algorithm. The result is shown in Figure 4 along with the traditional location result. There are two obvious differences between these two results. First, the event cluster 1 was shifted from the elevation of  $-2.06$  km to approximately  $-2.15$  km. Second, the event cluster 2 was shifted to a lower position and is flatter than the original one. In the following “Result verification” section, we first verify the improved accuracy for these two clusters with angle of incidence and arrival time match. Then, we show the stableness of the inversion with a cross-validation. Finally, we quantify the location uncertainty with perforation shots.

### Result verification

#### Improved match in angles of incidence

Using event 1 in cluster 1 as an example, we show our improved match in angle of incidence. Because the angle of incidence is independent of the arrival time information we used for inversion, it provides a quality control cross check for the estimated locations. Specifically, we calculate the angle of incidence using the P-wave polarization for each source-receiver pair. Then, with the provided and simultaneous inverted velocity models, we built two maps of angle of incidence misfit as shown in Figure 5. From Figure 5a, we can see that the location estimated using the traditional method results in a misfit of  $18^\circ$ , which is a relatively large value. The

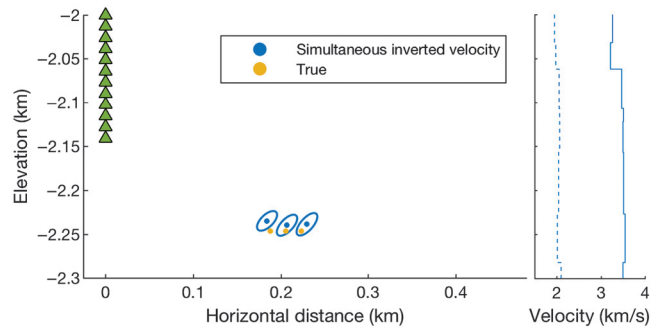
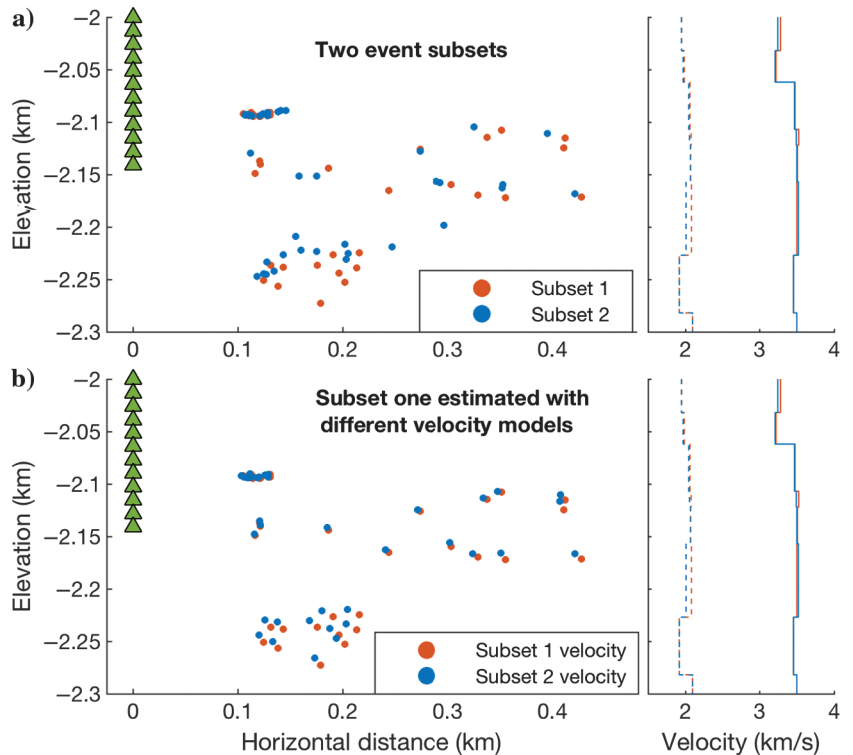


Figure 10. Perforation shot locations estimated with the velocity model simultaneous inverted with the 76 events. Ellipses are 95% confidence intervals of the estimation. The right panel shows the velocity model. The solid line is for  $V_p$ , and the dashed line is for  $V_s$ .

Figure 9. (a) Subset one (orange dots) and subset two (blue dots) events for the cross-validation. The right panel shows the velocity models estimated with subset-one (orange lines) and subset-two events (blue lines), respectively. The solid lines are for  $V_p$ , and the dashed lines are for  $V_s$ . (b) Subset-one event locations estimated using the two velocity models from (a). These two results match relatively well.



simultaneously inverted location is able to reduce the misfit to 8° (Figure 5b). The observed and predicted angles of incidence at each geophone are compared in Figure 6. The comparison shows that the

updated model significantly improved the match between observed and predicted angle of incidence. Admittedly, given the possible anisotropy of the earth, P-wave polarization may not be exactly the same as raypath direction (Thomsen, 1986). However, the difference due to anisotropy is a second-order effect because the misfit between the observed and predicted angles of incidence in this study is significantly larger.

*Improved match in arrival times*

We present the improvement in arrival time match using event 2 in cluster 2 as an example. Figure 7 shows the picked and predicted arrival times of this event. The waveforms have been rotated to show only the P- and SH-wave component. From the comparison, we can see the predicted arrival times of the traditional method deviated more from the picked arrival times. More importantly, they are unable to capture the moveouts of the picked arrival times. However, the simultaneous inversion algorithm was able to correct these misfits by updating the velocity model using arrival time information.

We compared the mean, SD, and root-mean-square (rms) of these arrival-time misfits of the 78 events in Table 1. The rms misfit of the traditional location method is 1.68 ms, whereas that of the simultaneous inversion is only 0.47 ms. Figure 8 shows the histogram of these misfits. The one for the simultaneous inversion is much more

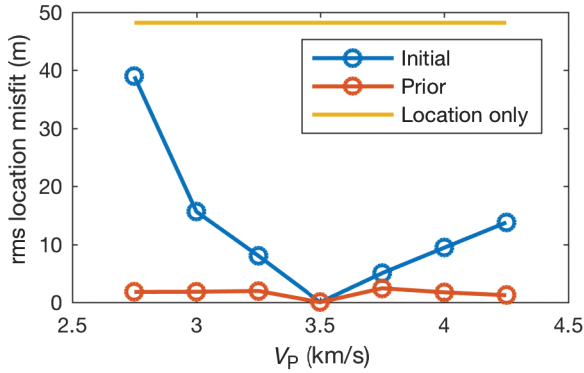


Figure 11. An rms location difference introduced by varying the initial (blue line) or prior (orange line)  $V_p$  values. The initial or prior  $V_s$  values were adapted according to a  $V_p/V_s$  of 1.67. When the initial  $V_p$  value is between 3.0 and 4.0 km/s, which is a reasonable range according to the sonic log in Figure 3, the rms difference is well below 15 m. The yellow line shows the rms difference between the event location estimated by simultaneous inversion and traditional location methods.

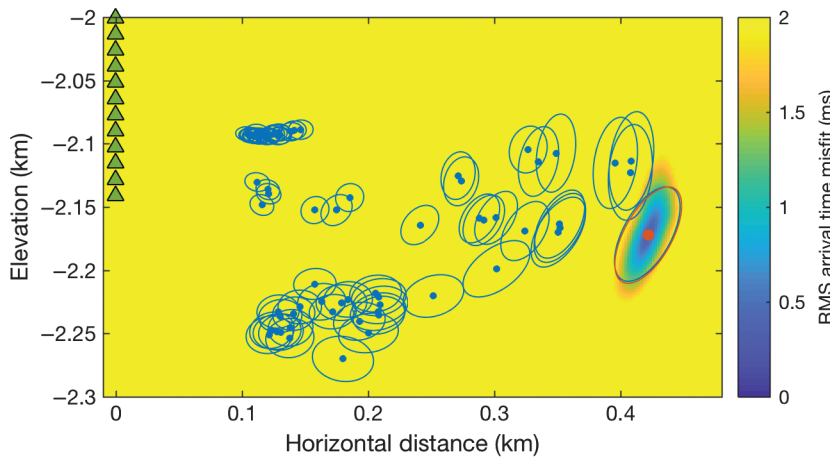


Figure 12. The MAP locations estimated by simultaneous inversion and the 95% confidence regions (ellipses) predicted by the Bayesian inference. The colored background is a map of arrival time misfit for the orange event (event 1 in Figure 4), which is a traditional way to quantify location uncertainty. The relatively good match between these two results verifies the effectiveness of Bayesian inference in uncertainty analysis.

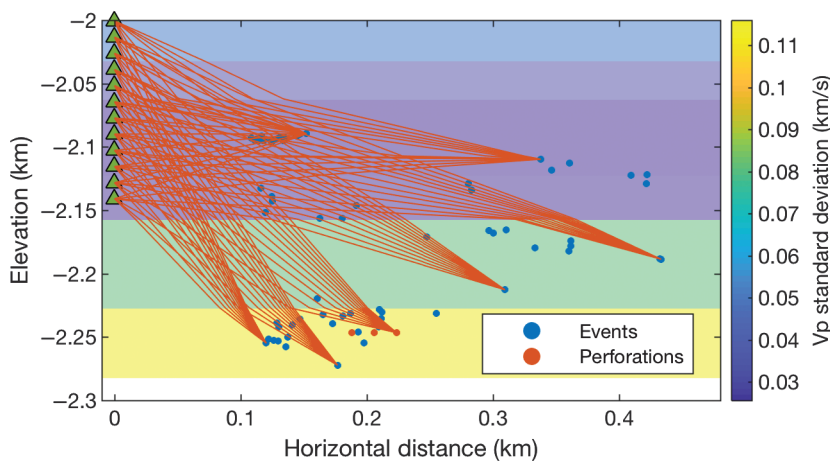


Figure 13. The raypaths from several representative events to the geophone array. The colored background is the SD of the velocity model estimation uncertainty. The uncertainty of the velocity model tends to be larger as the model goes deeper.

concentrated around zero. This large decrease in rms misfit attributes to the improvement in arrival time match like Figure 7.

A common ambiguity in simultaneous inversion is whether the improved arrival time match is a result of improved velocity model or just a result of overfitting. To prove that the reduction in rms misfit is not due to overfitting, we carried out a cross-validation test as shown in the following section.

#### Cross-validation

We randomly divided the 76 events into two subsets with 38 events each. We then applied the simultaneous inversion independently to these two subsets. The event locations and velocity models obtained are shown in Figure 9a. The two velocity models match each other well, especially at the depth around the geophone array. In addition, as shown in Table 1, the rms misfit of arrival times for these two subsets are 0.44 and 0.48 ms, respectively, which are similar to the rms misfit of 0.47 ms for the whole 76 event set. Finally, using the velocity model estimated from *subset-two events*, we located *the events of subset one* with the traditional location method. The result compares well with the simultaneously inverted one using only subset-one events as shown in Figure 9b. This means that the velocity model estimated independently from subset one events fits the arrival times of these events better than the provided velocity model. It confirms the reduction in arrival time misfit is not due to overfitting but to an improved velocity model.

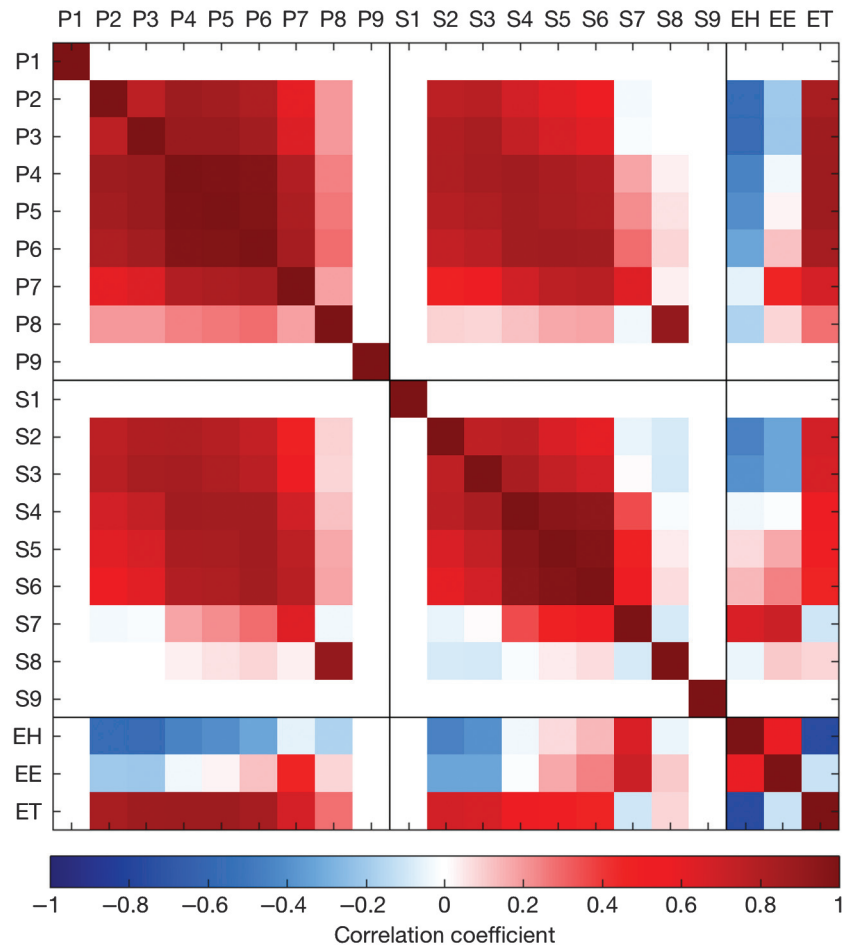
#### Locating perforation shots

We quantified the location uncertainty by locating the perforation shots to compare with their true locations (Figure 10). The velocity model we used is inverted using the 76 events. The arrival time misfit of the perforation shots is 0.88 ms as shown in Table 1. The rms location misfit of these shots is approximately 10 m, which represents the location uncertainty that we can achieve with our inverted velocity model in the 2D domain.

#### Effect of prior and initial model

A simultaneous inversion can be a highly nonlinear problem. Also, there are potential trade-offs among model parameters. The inversion result might be affected by the prior model or the initial guess before iteratively minimizing the objective function. To investigate these effects, we tested with various prior and initial velocity models. The rms difference between these results and the one we adopted in this paper is shown in Figure 11. The range of  $V_P$  values we analyzed is 2.75–4.25 km/s. The initial or prior  $V_S$  values were adapted according to  $V_P/V_S$  of 1.67. When the initial velocity value is between 3.0 and 4.0 km/s, which is a reasonable range according to the sonic log in Figure 3, the rms difference is well below 15 m. This is significantly smaller than the difference between simultaneous and traditional location methods. The rms location difference introduced by varying the prior velocity model is less than 3 m

Figure 14. Correlation matrix of the  $V_P$ ,  $V_S$  of each layer and horizontal distance, elevation, and origin time of event 1 in Figure 4. P1–P9 stand for  $V_P$  values from the shallowest layer to the deepest layer; S1–S9 stand for  $V_S$  values of these layer; EH, EE, and ET are the horizontal source-receiver distance, elevation, and origin time of event 1, respectively.



thanks to our choice of 2.0 km/s as the velocity SD. The location difference introduced by varying the initial and prior event locations is trivial and is not shown here for simplicity. From this analysis, we conclude that the choice of prior or initial model will not significantly affect the inversion result for this data set.

**Uncertainty analysis and posterior covariance**

A traditional way to quantify location uncertainty is calculating an arrival-time misfit map. However, this can be computationally intensive for simultaneous inversion because of the increased number of model parameters. The Bayesian inversion is able to provide an estimation of posterior uncertainty of model parameters with little extra cost. Figure 12 shows the 95% confidence region predicted by the Bayesian inference. In Figure 12, we also compare this uncertainty estimation with the misfit map using event 1 as an example. The good match between these two results verifies the effectiveness of Bayesian inference in terms of uncertainty analysis. Figure 13 shows the posterior P-wave velocity model uncertainty along with the raypaths of several representative events. The S-wave velocity uncertainty shares similar trend with that of the P-wave and is not shown for simplicity. The model uncertainty around the elevation of the geophone array is relatively small, whereas that below the geophone array is large due to poor raypath coverage. Because the uncertainties of event locations and velocities increase as they go deeper (Figures 12 and 13), we would suggest to have the geophone array to straddle the stimulation zone in a survey whenever possible. This will increase the accuracy of microseismic event location and velocity model estimation.

The Bayesian inference is also able to capture the correlation among model parameters (Poliannikov et al., 2013; Zhang et al., 2017). Figure 14 shows the posterior correlation matrix of the velocity model, location, and origin time of event 2. It provides insights into the trade-offs and correlations between various parameter pairs. For instance, a smaller  $V_P$  results in smaller  $V_P/V_S$ . For a given P-S separation time, it leads an event to be located further away from the geophone array. This is reflected in the negative correlation between the horizontal distance and the  $V_P$  values. The positive correlation between elevation and horizontal distance of event 1 gives the orientation of the confidence ellipse in Figure 12.

**Result of the entire data set**

Finally, we show the inversion result of all the detected microseismic events in stage 1 and stage 5. Events from stage 1A, stage 1B, and stage 5 are inverted separately. The azimuthal raypath coverage of these events is shown in Figure 2b. Here, we used the picks provided by the contractor instead of our own picks. We also added the azimuthal information provided by the contractor to show locations in 3D space. The result is shown in Figure 15a with the events color coded with their corresponding stages. We also located these events with the traditional location method. Its comparison with the simultaneous inversion is shown in Figure 15b.

Figure 16a shows the side view of stage 1B events. From this comparison, there is a vertical shift for a subset of events, which is consistent with the shift of cluster 1 in Figure 4. Figure 16b and 16c are event locations color coded with origin times estimated with the traditional method and simultaneous inversion, respectively. From

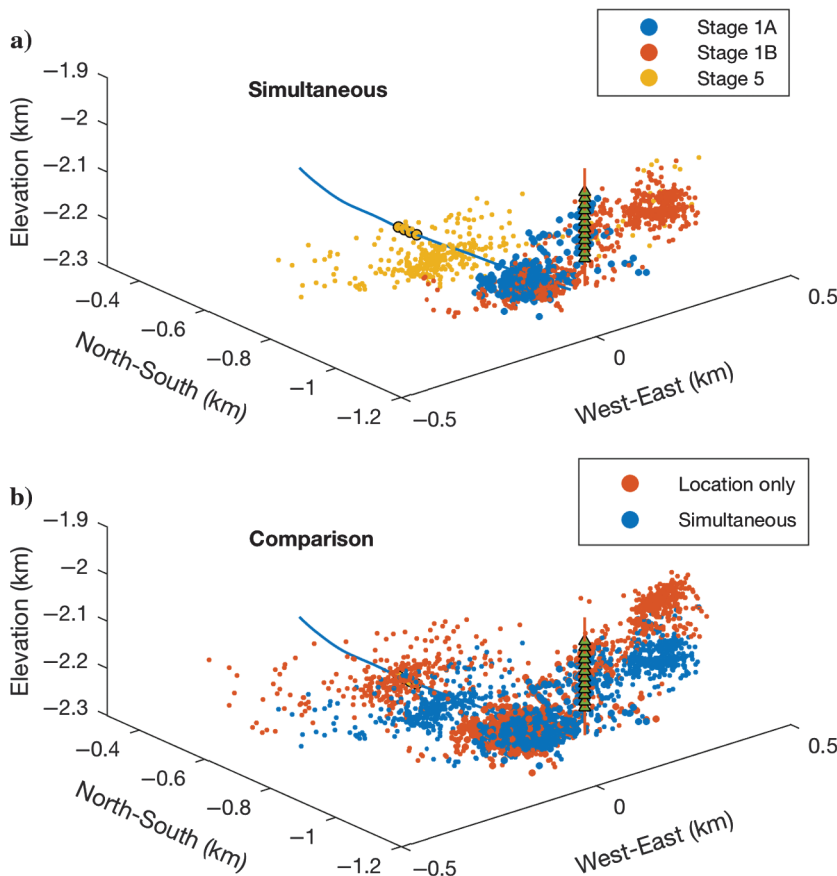


Figure 15. (a) Microseismic event locations estimated by simultaneous inversion for stages 1A, 1B, and 5. The events are color coded with their corresponding stages. (b) Event locations estimated with simultaneous inversion (blue dots) and those estimated with the traditional method (orange dots).

the comparison, we can tell the events estimated with simultaneous inversion are more clustered, which might be an indication of improved accuracy. Similar with Figure 16, Figure 17 shows the map view of stage 5 events. There is a horizontal shift of approximately 100 m in stage 5 events between the two methods. Similar with stage 1, we also found the events are more clustered in the simultaneous inversion result. The two results will lead to different interpretations. Figure 17b shows that the early events occurred at the north side of the target stimulation zone, and they gradually propagated to the south as the stimulation continues. Figure 17c shows that the early events occurred at the south end of the target stimulation zone, and they gradually propagate to the south side.

### VELOCITY MODELS

One advantage of simultaneous inversion is its possibility to estimate variant velocity models for different event subsets. We compared the velocity models estimated with events from different

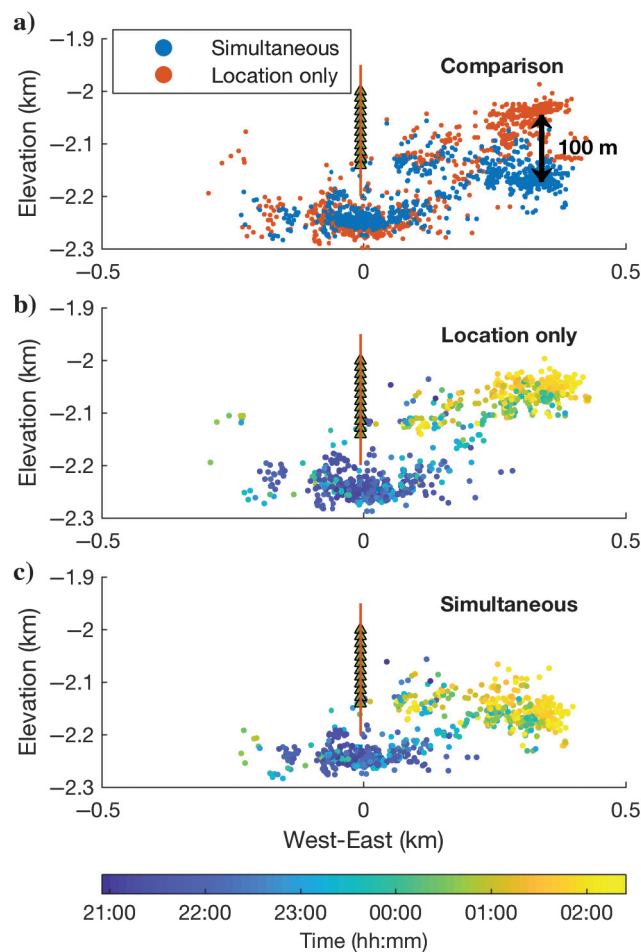


Figure 16. (a) Side view of stage 1B events estimated with simultaneous inversion (blue dots) and those estimated with the traditional method (orange dots). There is a vertical shift of approximately 100 m in an event cluster. This is consistent with the shift of cluster 1 in Figure 4. (b and c) These two results color coded with the event origin times. Compared with the events in (b), those in (c) are more clustered, which might be an indication of the improved event location accuracy.

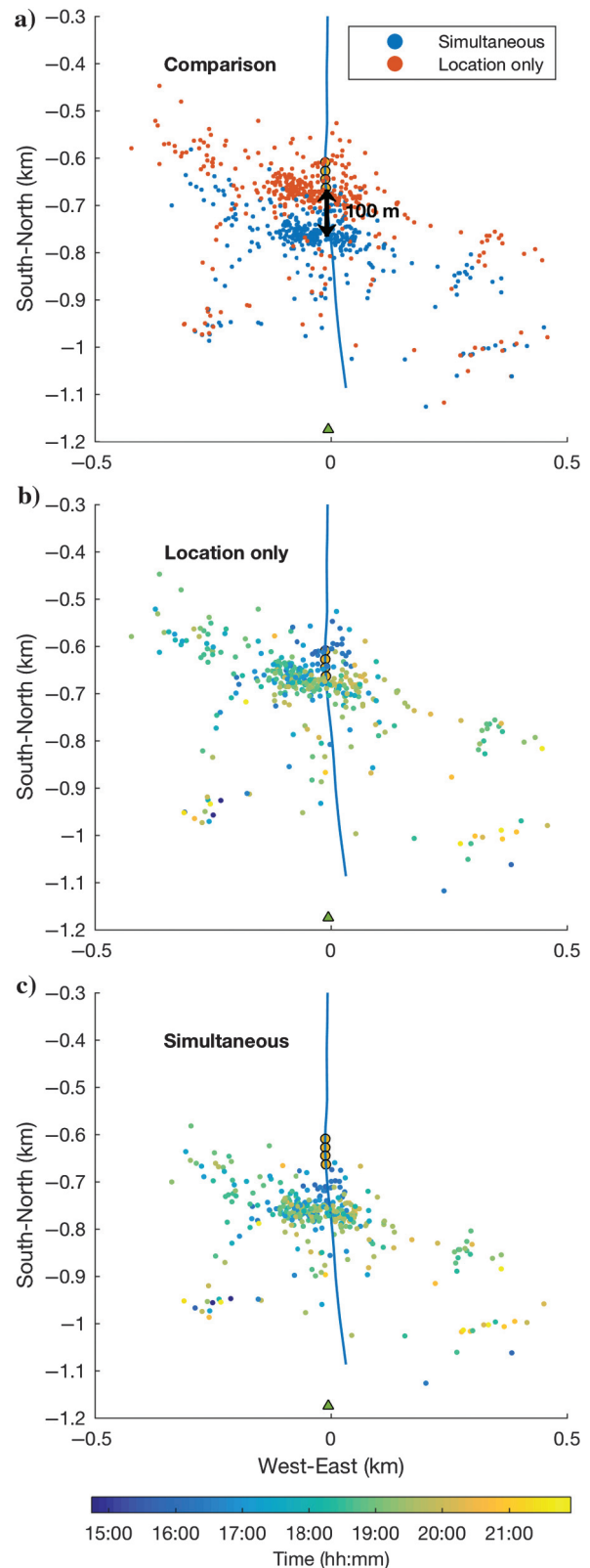


Figure 17. The same as Figure 16 but the map view of stage 5 events. There is a horizontal shift of approximately 100 m for most of the events. Compared with the events in (b), those in (c) are more clustered.

stimulation stages and their associated  $V_P/V_S$  as shown in Figure 18. The interval in which there are raypath coverages for stage 1 and stage 5 is between the elevation of  $-2.0$  and  $-2.23$  km. From the comparison of the velocity models within this interval, the  $V_P/V_S$  is systematically lower for stage 5 than for stage 1. One possible explanation to this change in the reservoir properties is the effect of hydraulic fracturing. Indeed, hydrofractures tend to result in reduced  $V_P/V_S$  or Poisson's ratio (Mavko et al., 2009). This is consistent with our inverted velocity models. An alternative explanation is the inherent lateral heterogeneity of the reservoir itself. That is, the property of the formation may change horizontally from stage 1 to stage 5. However, further study needs to be carried out to understand the real cause of this change, and simultaneous inversion is a promising tool to do so. As a reference, the gray lines in the background of Figure 18 are sonic logs from the observation well. The  $V_P/V_S$  of the inverted models for stages 1A and 1B match the sonic log reasonably well. Possible reasons for discrepancies at certain intervals include anisotropy, spatial heterogeneity (the sonic log is a survey in 1D, whereas the simultaneous inverted model is an effective velocity model of a 3D earth), and stimulation induced rock property change.

DISCUSSION

One thing that is important for unconventional reservoirs but not considered in this study is anisotropy. Clear evidence of anisotropy for various shale formations have been presented (Warpinski et al., 2009). Previous studies have been carried out to estimate vertical transverse isotropy (Du and Warpinski, 2013; Li et al., 2013, 2014), azimuthal anisotropy (Grechka and Yaskovich, 2014), and homogeneous triclinic (Grechka and Duchkov, 2011; Grechka et al., 2011) models. The moveout of arrival times can be affected by anisotropy, thus leading to a biased isotropic velocity model in simultaneous inversion. Indeed, we have observed S-wave splitting phenomena in the microseismic waveforms, which makes the isotropic assumption in this work less solid. The simultaneous inversion method used in this paper can also be used to estimate anisotropy parameters, which will be our future work.

The velocity model is usually a major source of uncertainty in a microseismic event location problem. However, depending on the setup of a survey, various factors may dominate location errors. Statics may cause a problem for a highly weathered area in a surface microseismic survey. The orientations of the geophones may need to be calibrated in cases in which no perforation shot is available. Thanks to the power of Bayesian inference, these factors may be accounted for as model parameters depending on the necessity of a specific survey and availability of observations. The inclusion of these crucial parameters in a model to be estimated reduces the risk of bias introduced by inaccurate models. Also, various observations, such as P-wave polarization, S-wave splitting, reflected and refracted waves, can be used to improve event location accuracy.

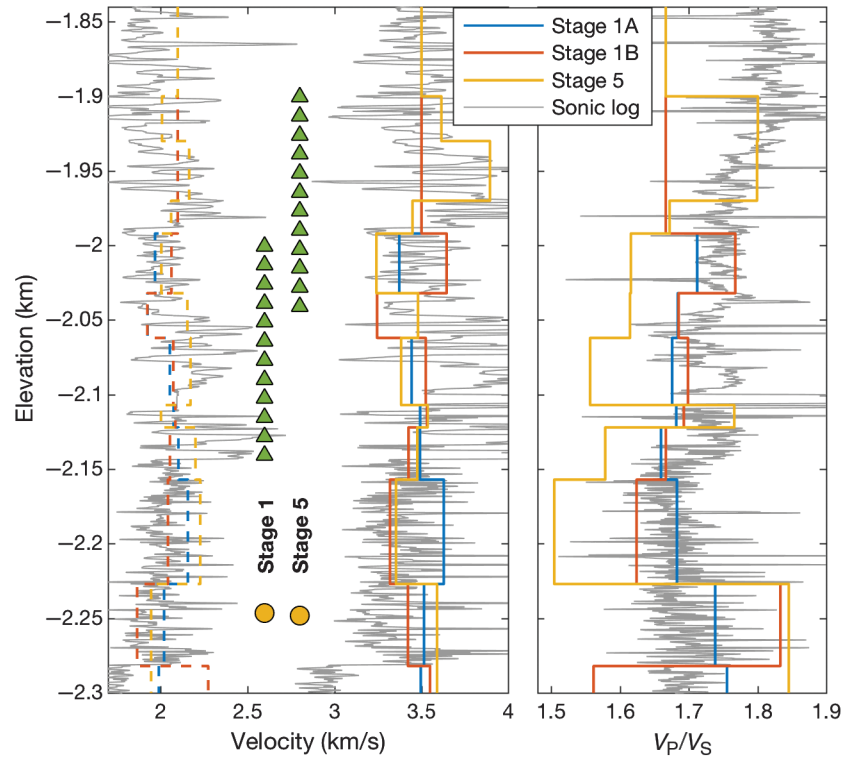


Figure 18. Simultaneously inverted velocity models and their corresponding  $V_P/V_S$ . The solid lines are for  $V_P$ , and the dashed lines are for  $V_S$ . The green triangles and yellow circles represent the elevations of geophones and the perforation shots, respectively. Comparing the  $V_P/V_S$  between the elevation of  $-2.0$  and  $-2.23$  km, where there is relatively good raypath coverage for all stages, we can see the  $V_P/V_S$  is higher for stage 5 than that of stage 1. The velocity model of stages 1A and 1B above the elevation of  $-2.0$  km stays at the prior/initial velocity model due to lack of raypath coverage.

The consideration of these factors should be on a case-by-case basis depending on the specific situation and data quality of a survey.

From this study (Figure 18), a stage-dependent earth model is necessary due to the possible effects of the fracturing-induced change, horizontal heterogeneity, or intrinsic anisotropy of the formation. Simultaneous inversion provides the potential to construct data-dependent velocity models given the abundance of microseismic events in most surveys. Integrated with rock-physics models, the space- or time-dependent earth models can be used to characterize hydrofracture properties or horizontal heterogeneity of the formation. It may also be used to validate or calibrate a rock-physics model for fractured rocks.

CONCLUSION

We simultaneously inverted for the velocity model and microseismic event locations in the Vaca Muerta Formation. Bayesian inference provides a quantification of estimation uncertainty and correlation among model parameters. The result was compared with locations estimated with a traditional method. The final velocity model and event locations are improved in terms of accuracy. The improvement has been verified by different analyses, such as the improved match in angles of incidence and arrival times. The stability of the inversion was tested with a cross-validation. Simultaneous inversion is an effective way to use information from microseismic data to construct stage-dependent velocity models. With the algorithm demonstrated in this

paper, we can perform microseismic monitoring to fracturing treatments in which no perforation data is available. In addition, it could be applied to reservoir monitoring when we need to retrieve velocity information from microseismic events themselves.

## ACKNOWLEDGMENTS

The authors would like to thank Total S. A. and Total Austral and its partners for granting permission to publish this paper.

## REFERENCES

- Aki, K., and P. G. Richards, 1980, Quantitative seismology: Theory and methods: W. H. Freeman and Company.
- Artman, B., I. Podladtchikov, and B. Witten, 2010, Source location using time-reverse imaging: *Geophysical Prospecting*, **58**, 861–873, doi: [10.1111/j.1365-2478.2010.00911.x](https://doi.org/10.1111/j.1365-2478.2010.00911.x).
- Artman, B., and B. Witten, 2011, Wave-equation microseismic imaging and event selection in the image domain: 81st Annual International Meeting, SEG, Expanded Abstracts, 1699–1703, doi: [10.1190/1.3627531](https://doi.org/10.1190/1.3627531).
- Box, G. E., and G. C. Tiao, 2011, Bayesian inference in statistical analysis: John Wiley & Sons.
- Douglas, A., 1967, Joint epicentre determination: *Nature*, **215**, 47–48, doi: [10.1038/215047a0](https://doi.org/10.1038/215047a0).
- Drew, J. E., H. D. Leslie, P. N. Armstrong, and G. Michard, 2005, Automated microseismic event detection and location by continuous spatial mapping: Presented at the SPE Annual Technical Conference and Exhibition, SPE 95513-MS, doi: [10.2118/95513-MS](https://doi.org/10.2118/95513-MS).
- Du, J., and N. R. Warpinski, 2013, Velocity building for microseismic hydraulic fracture mapping in isotropic and anisotropic media: Presented at the SPE Hydraulic Fracturing Technology Conference, SPE 163866-MS, doi: [10.2118/163866-MS](https://doi.org/10.2118/163866-MS).
- Duncan, P. M., and L. Eisner, 2010, Reservoir characterization using surface microseismic monitoring: *Geophysics*, **75**, no. 5, 75A139–75A146, doi: [10.1190/1.3467760](https://doi.org/10.1190/1.3467760).
- Eisner, L., P. M. Duncan, W. M. Heigl, and W. R. Keller, 2009, Uncertainties in passive seismic monitoring: *The Leading Edge*, **28**, 648–655, doi: [10.1190/1.3148403](https://doi.org/10.1190/1.3148403).
- Eisner, L., and J. H. Le Calvez, 2007, New analytical techniques to help improve our understanding of hydraulically induced microseismicity and fracture propagation: Presented at the SPE Annual Technical Conference and Exhibition, SPE 110813-MS, doi: [10.2118/110813-MS](https://doi.org/10.2118/110813-MS).
- Garcia, M. N., F. Sorenson, J. C. Bonapace, F. Motta, C. Bajuk, and H. Stockman, 2013, Vaca Muerta Shale reservoir characterization and description: The starting point for development of a Shale play with very good possibilities for a successful project: Presented at the Unconventional Resources Technology Conference, URTEC 1508336-MS, doi: [10.1190/urtec2013-090](https://doi.org/10.1190/urtec2013-090).
- Gesret, A., N. Desassis, M. Noble, T. Romary, and C. Maisons, 2015, Propagation of the velocity model uncertainties to the seismic event location: *Geophysical Journal International*, **200**, 52–66, doi: [10.1093/gji/ggu374](https://doi.org/10.1093/gji/ggu374).
- Grechka, V., and A. A. Duchkov, 2011, Narrow-angle representations of the phase and group velocities and their applications in anisotropic velocity-model building for microseismic monitoring: *Geophysics*, **76**, no. 6, WC127–WC142, doi: [10.1190/geo2010-0408.1](https://doi.org/10.1190/geo2010-0408.1).
- Grechka, V., and W. M. Heigl, 2017, Microseismic monitoring: SEG.
- Grechka, V., P. Singh, and I. Das, 2011, Estimation of effective anisotropy simultaneously with locations of microseismic events: *Geophysics*, **76**, no. 6, WC143–WC155, doi: [10.1190/geo2010-0409.1](https://doi.org/10.1190/geo2010-0409.1).
- Grechka, V., and S. Yaskevich, 2013, Inversion of microseismic data for triclinic velocity models: *Geophysical Prospecting*, **61**, 1159–1170, doi: [10.1111/1365-2478.12042](https://doi.org/10.1111/1365-2478.12042).
- Grechka, V., and S. Yaskevich, 2014, Azimuthal anisotropy in microseismic monitoring: A Bakken case study: *Geophysics*, **79**, no. 1, KS1–KS12, doi: [10.1190/geo2013-0211.1](https://doi.org/10.1190/geo2013-0211.1).
- Jansky, J., V. Plicka, and L. Eisner, 2010, Feasibility of joint 1D velocity model and event location inversion by the neighbourhood algorithm: *Geophysical Prospecting*, **58**, 229–234, doi: [10.1111/j.1365-2478.2009.00820.x](https://doi.org/10.1111/j.1365-2478.2009.00820.x).
- Li, C., T. Dohmen, S. Morton, K. Katahara, K. Hayles, S. Checkles, and J. Blangy, 2012, Evaluating the quality of microseismic event locations: 82nd Annual International Meeting, SEG, Expanded Abstracts, doi: [10.1190/segam2012-1155.1](https://doi.org/10.1190/segam2012-1155.1).
- Li, J., C. Li, S. A. Morton, T. Dohmen, K. Katahara, and M. N. Toksöz, 2014, Microseismic joint location and anisotropic velocity inversion for hydraulic fracturing in a tight Bakken reservoir: *Geophysics*, **79**, no. 5, C111–C122, doi: [10.1190/geo2013-0345.1](https://doi.org/10.1190/geo2013-0345.1).
- Li, J., H. Zhang, W. L. Rodi, and M. N. Toksoz, 2013, Joint microseismic location and anisotropic tomography using differential arrival times and differential backazimuths: *Geophysical Journal International*, **195**, 1917–1931, doi: [10.1093/gji/ggt358](https://doi.org/10.1093/gji/ggt358).
- Mavko, G., T. Mukerji, and J. Dvorkin, 2009, The rock physics handbook: Tools for seismic analysis of porous media: Cambridge University Press.
- Maxwell, S., 2009, Microseismic location uncertainty: *CSEG Recorder*, **34**, 41–46.
- Maxwell, S., 2014, Microseismic imaging of hydraulic fracturing: Improved engineering of unconventional shale reservoirs: SEG.
- Myers, S. C., G. Johannesson, and W. Hanley, 2007, A Bayesian hierarchical method for multiple-event seismic location: *Geophysical Journal International*, **171**, 1049–1063, doi: [10.1111/j.1365-246X.2007.03555.x](https://doi.org/10.1111/j.1365-246X.2007.03555.x).
- Myers, S. C., G. Johannesson, and W. Hanley, 2009, Incorporation of probabilistic seismic phase labels into a Bayesian multiple-event seismic locator: *Geophysical Journal International*, **177**, 193–204, doi: [10.1111/j.1365-246X.2008.04070.x](https://doi.org/10.1111/j.1365-246X.2008.04070.x).
- Poliannikov, O. V., M. Prange, A. Malcolm, and H. Djikpesse, 2013, A unified Bayesian framework for relative microseismic location: *Geophysical Journal International*, **194**, 557–571, doi: [10.1093/gji/ggt119](https://doi.org/10.1093/gji/ggt119).
- Poliannikov, O. V., M. Prange, A. E. Malcolm, and H. Djikpesse, 2014, Joint location of microseismic events in the presence of velocity uncertainty: *Geophysics*, **79**, no. 6, KS51–KS60, doi: [10.1190/geo2013-0390.1](https://doi.org/10.1190/geo2013-0390.1).
- Rohmer, B., M. Raverta, J. L. Boutaud de la Combe, and V. Jaffrezic, 2015, Minifrac analysis using well test technique as applied to the Vaca Muerta Shale play: Presented at the SPE Europec, SPE 174380-MS, doi: [10.2118/174380-MS](https://doi.org/10.2118/174380-MS).
- Rutledge, J. T., and W. S. Phillips, 2003, Hydraulic stimulation of natural fractures as revealed by induced microearthquakes, Carthage Cotton Valley gas field, east Texas: *Geophysics*, **68**, 441–452, doi: [10.1190/1.1567214](https://doi.org/10.1190/1.1567214).
- Sagasti, G., A. Ortiz, D. Hryb, M. Foster, and V. Lazzari, 2014, Understanding geological heterogeneity to customize field development: An example from the Vaca Muerta unconventional play, Argentina: Presented at the Unconventional Resources Technology Conference, URTEC 1923357-MS, doi: [10.15530/URTEC-2014-1923357](https://doi.org/10.15530/URTEC-2014-1923357).
- Song, F., and M. N. Toksöz, 2011, Full-waveform based complete moment tensor inversion and source parameter estimation from downhole microseismic data for hydrofracture monitoring: *Geophysics*, **76**, no. 6, WC103–WC116, doi: [10.1190/geo2011-0027.1](https://doi.org/10.1190/geo2011-0027.1).
- Tarantola, A., 2005, Inverse problem theory and methods for model parameter estimation: SIAM.
- Tarantola, A., and B. Valette, 1982, Inverse problems—Quest for information: *Journal of Geophysics*, **50**, 159–170.
- Thomsen, L., 1986, Weak elastic anisotropy: *Geophysics*, **51**, 1954–1966, doi: [10.1190/1.1442051](https://doi.org/10.1190/1.1442051).
- Waldhauser, F., and W. L. Ellsworth, 2000, A double-difference earthquake location algorithm: Method and application to the northern Hayward fault, California: *Bulletin of the Seismological Society of America*, **90**, 1353–1368, doi: [10.1785/0120000006](https://doi.org/10.1785/0120000006).
- Warpinski, N., 2009, Microseismic monitoring: Inside and out: *Journal of Petroleum Technology*, **61**, 80–85, doi: [10.2118/118537-JPT](https://doi.org/10.2118/118537-JPT).
- Warpinski, N. R., C. K. Waltman, J. Du, and Q. Ma, 2009, Anisotropy effects in microseismic monitoring: Presented at the SPE Annual Technical Conference and Exhibition, SPE 124208-MS, doi: [10.2118/124208-MS](https://doi.org/10.2118/124208-MS).
- Zhang, H., S. Sarkar, M. N. Toksöz, H. S. Kuleli, and F. Al-Kindy, 2009, Passive seismic tomography using induced seismicity at a petroleum field in Oman: *Geophysics*, **74**, no. 6, WCB57–WCB69, doi: [10.1190/1.3253059](https://doi.org/10.1190/1.3253059).
- Zhang, Z., B. Jafarpour, and L. Li, 2014, Inference of permeability heterogeneity from joint inversion of transient flow and temperature data: *Water Resources Research*, **50**, 4710–4725, doi: [10.1002/2013WR013801](https://doi.org/10.1002/2013WR013801).
- Zhang, Z., J. W. Rector, and M. J. Nava, 2017, Simultaneous inversion of multiple microseismic data for event locations and velocity model with Bayesian inference: *Geophysics*, **82**, no. 3, KS27–KS39, doi: [10.1190/geo2016-0158.1](https://doi.org/10.1190/geo2016-0158.1).